Effects of Strain State and Strain Rate on Deformation-Induced Transformation in 304 Stainless Steel: Part I. Magnetic Measurements and Mechanical Behavior

S. S. HECKER, M. G. STOUT, K. P. STAUDHAMMER, and J. L. SMITH

The $\gamma \to \alpha'$ transformation in 304 stainless steel can be induced by plastic deformation at room temperature. The kinetics of strain-induced transformations have been modeled recently by Olson and Cohen. We used magnetic techniques to monitor the progress of the $\gamma \to \alpha'$ transformation in 304 stainless steel sheet loaded in uniaxial and biaxial tension at both low (10^{-3} per second) and high (10^3 per second) strain rates. We found that using the von Mises effective strain criterion gives a reasonable correlation of transformation kinetics under general strain states. The principal effect of increased strain rate was observed at strains greater than 0.25. The temperature increase resulting from adiabatic heating was sufficient to suppress the $\gamma \to \alpha'$ transformation substantially at high rates. The consequences of the $\gamma \to \alpha'$ transformation on mechanical behavior were noted in uniaxial and biaxial tension. Uniaxial tension tests were conducted at temperatures ranging from 50 to -80 °C. We found that both the strain hardening and transformation rates increased with decreasing temperature. However, the martensite transformation saturates at ~ 85 pct volume fraction α'. This can occur at strains less than 0.3 for conditions where the transformation is rapid. Once saturation occurs, the work hardening rate decreases rapidly and premature local plastic instability results. In biaxial tension, the same tendency toward plastic instability associated with high transformation rates provides a rationale for the low biaxial ductility of 304 stainless steel.

I. INTRODUCTION

A complete constitutive description of material behavior requires information about a material's response as a function of strain, stress (or strain) state, strain rate, and temperature. Of these variables strain state and strain rate have been studied least. In this two-part series we examine the evolution of microstructure in 304 stainless steel as a function of strain, strain state, and strain rate. We consider the understanding of microstructural evolution to hold the key for an eventual understanding of the complete flow and failure behavior. We chose 304 stainless steel for this study because of its obvious practical importance and because of the multitude of microstructural phenomena that occur during plastic deformation.

We studied only the evolution of microstructure with strain and not the stress-strain response because the test techniques used to generate multiaxial loading and high strain-rate deformation did not permit meaningful load measurements. The microstructures produced under all loading conditions were studied principally by transmission electron microscopy (TEM), and the results of this study constitute Part II. We found that at moderate-to-large plastic deformation, strain-induced martensite was the most significant microstructural change. The progress of the martensitic transformation was followed by magnetic techniques. These results and the mechanical test results are discussed in Part I.

When 304 stainless steel is deformed at room temperature it transforms martensitically from fcc austenite (γ) to bcc martensite (α'). This transformation has been studied extensively in uniaxial tension at low strain rates.[1-11] Early work

by Mathieu,[12] Form and Baldwin,[13] and Powell et al[5] at moderately high strain rates showed that the amount of martensite decreased with increasing rate. Powell et al[5] and later Bressanelli and Moskowtiz[9] and Neff et al[14] concluded that the increased stability of the austenite resulted from adiabatic heating at high rates. An understanding of the total elongation achieved in austenitic stainless steels is complicated by the strain-induced transformation[6,14,15] which, in turn, depends on alloy chemistry, temperature, and strain rate. The influence of stress (strain) state on transformation has received very little attention. Patel and Cohen[16] showed that both the shear stress and the normal stress components are important. In all cases the shear stress aids the transformation. The normal stress can either aid or hinder the transformation, depending on whether or not it is in the direction of the volume change of the transformation. Powell et al[5] showed that uniaxial tensile stresses favored the $\gamma \to \alpha'$ transformation more than uniaxial compression, although α' formed in both cases because of the shear stresses. The influence of torsion was similar to that of compression.

In this study we conducted a systematic series of experiments to assess the influence of both strain rate and strain state. We examine the results in terms of the Olson-Cohen theory for strain-induced transformation kinetics[17] and propose a simple extension of their theory to predict transformation kinetics under multiaxial loading.

II. DEFORMATION-INDUCED TRANSFORMATION IN 304 STAINLESS STEEL

The crystallography of the $\gamma \to \alpha'$ transformation and its dependence on alloy chemistry and temperature are fairly well established. The transformation in 304 stainless steel is considered to be strain-induced in contrast to stress-assisted.[10,11] In strain-induced transformations plastic deformation of the parent phase creates the proper defect structure

which acts as an embryo for the transformation product. Specifically, in austenitic stainless steels embryos are formed at the intersections of microscopic shear bands, e.g., stacking faults, twins, and hcp ε martensites.[3,4,7] The morphology of the transformation product is typically described as lath-like.[7,10] In stress-assisted transformations the embryos are considered to be the same as those that activate thermally-induced martensite with stress adding to the thermodynamic driving force, as explained by Patel and Cohen.[16] Typically, transformation of the parent phase occurs before plastic deformation takes place by dislocation multiplication or twinning. The stress-assisted transformation product is identical to thermally-induced martensite. In most steels the morphology of these products can be described as plate-like, or lenticular. However, it has been shown that in 18-8 stainless steels, even the thermally-induced martensite is lath-like.[18,19]

The kinetics of the strain-induced transformation have been modeled recently by Olson and Cohen.[17] They assume microscopic shear band intersections to be the dominant nucleation sites. They relate the volume fraction of shear bands, f^{sb}, to plastic strain, ε, by assuming a constant rate of consumption of shear-band-free volume. This gives

$$f^{sb} = 1 - \exp(-\alpha\varepsilon) \qquad [1]$$

where α depends on stacking fault energy and strain rate. The number of shear band intersections is related to the number of shear bands by the simple expression

$$N_v^I = K(N_v^{sb})^n \qquad [2]$$

where N_v^I is the number of intersections, N_v^{sb} the number of shear bands, and K and n are constants. The incremental increase in martensite embryos, dN_v^α, is then related to the increase in shear-band intersections by

$$dN_v^\alpha = p\,dN_v^I \qquad [3]$$

where p is the probability that a shear band intersection will form a martensite embryo. They assume further that the volume per martensite unit is constant, being restricted to the region of shear-band intersection. Hence, the total volume fraction of martensite depends on the number of embryos and is related to plastic strain by

$$f^{\alpha'} = 1 - \exp\{-\beta[1 - \exp(-\alpha\varepsilon)]^n\} \qquad [4]$$

where $\beta = (\bar{\nu}^{\alpha'})/(\bar{\nu}^{sb})^n\,Kp$ and $\bar{\nu}^{\alpha'}$ is the volume of an α' unit and $\bar{\nu}^{sb}$ the volume of a shear band. Eq. [4] predicts that the curve of volume fraction martensite as a function of strain has a sigmoidal shape, in agreement with the data of Angel.[1] We will compare our data to that of Angel and to the predictions of Olson and Cohen below. The Olson-Cohen analysis provides a rationale for the formation of martensite with plastic straining and how this is affected by stacking fault energy and strain rate.

III. EXPERIMENTAL

All work was performed on 304 stainless steel (18.12 pct Cr, 8.60 pct Ni, 0.055 pct C, 0.20 pct Co, 0.14 pct each of Cu, Mo, and W (all in wt pct) and the balance Fe) purchased from a commercial supplier as mill-annealed sheet, 0.178 mm thick. Optical metallography and transmission electron microscopy of the as-received material verified that it was annealed and had a grain size of ~15 μm.

A. Mechanical Testing

Uniaxial tensile tests. Low rate uniaxial tensile tests were conducted in an Instron machine at a strain rate of ~10^{-3} per second. The test specimens, with a gage length of 30 mm and width of 12.7 mm, were punched from the annealed sheet with a punch and die assembly. The edges were carefully prepared by filing, sanding, and electropolishing to eliminate the effects of cold work introduced during punching. A grid of circles 1.25 mm in diameter was copper plated onto all specimens using a photoresist technique. Strains were measured during testing with an extensometer and after testing by measuring the circle grids. Specimens were deformed to different strain levels ranging from two pct to failure. The specimens were subsequently used for magnetic measurements and transmission electron microscopy (TEM). In addition to the tests at room temperature, we tested specimens at -80, -15, and 50 °C to check the temperature dependence of the transformation.

Uniaxial testing at high strain rate (~10^3 per second) was conducted on specimens with a 12.7 mm gage length and 3.18 mm gage width in our Two-inch Gas Gun (TIG) facility. The details of the apparatus and test technique are described elsewhere.[20] Briefly, the specimen is gripped with wedge fixtures in a miniature reaction frame, as shown in Figure 1. The striker bar attached to the bottom end of the specimen is impacted with a tubular projectile at 45 m per second, causing the specimen to stretch and fail. The projectile is subsequently decelerated by impinging on an annealed copper ring. High-speed photographic measurements were made during the initial test setup to assure that the specimen end was actually accelerated to the projectile velocity. We controlled strain levels by notching the tensile specimens to different depths, causing them to fail prematurely after deforming to the desired strains. By using sharp notches near the bottom end of the specimen, we obtained large sections of specimens strained uniformly.

Biaxial tension tests. To achieve biaxial stress conditions we used the punch-stretch test described previously by Hecker.[21] Schematic diagrams of the two types of punch tests used are shown in Figure 2. For the case of the hemispherical punch test (Figure 2(a)), the specimen is held at the periphery and stretched over a rigid punch. The strain state is controlled by varying the lubrication or the specimen width.[21] To achieve balanced biaxial tension we used a 20 mm-thick spacer of polyurethane rubber between the specimen and rigid punch. This condition simulates hydraulic bulging, but is much more convenient, experimentally. For the in-plane punch test we used a flat, hollow-nosed punch, as shown in Figure 2(b). Stretching in this case occurs in the plane of the sheet without contact. Both of these tests were used to generate specimens stretched biaxially. The in-plane test has the advantage of providing large sections of a specimen with a uniform strain distribution. However, failure typically occurs over the radius of the punch nose and, hence, it is difficult to achieve high strain levels. Such strain levels were achieved using the hemispherical punch test. In both tests the strain levels were controlled by varying the depth of punch penetration on an MTS testing machine and the strains were measured with the circle grids.

We used only the hemispherical punch test at high strain rates because it is better suited for the gun operation. The setup was identical to that at low rate, except the hemispherical punch was part of the projectile launched into the
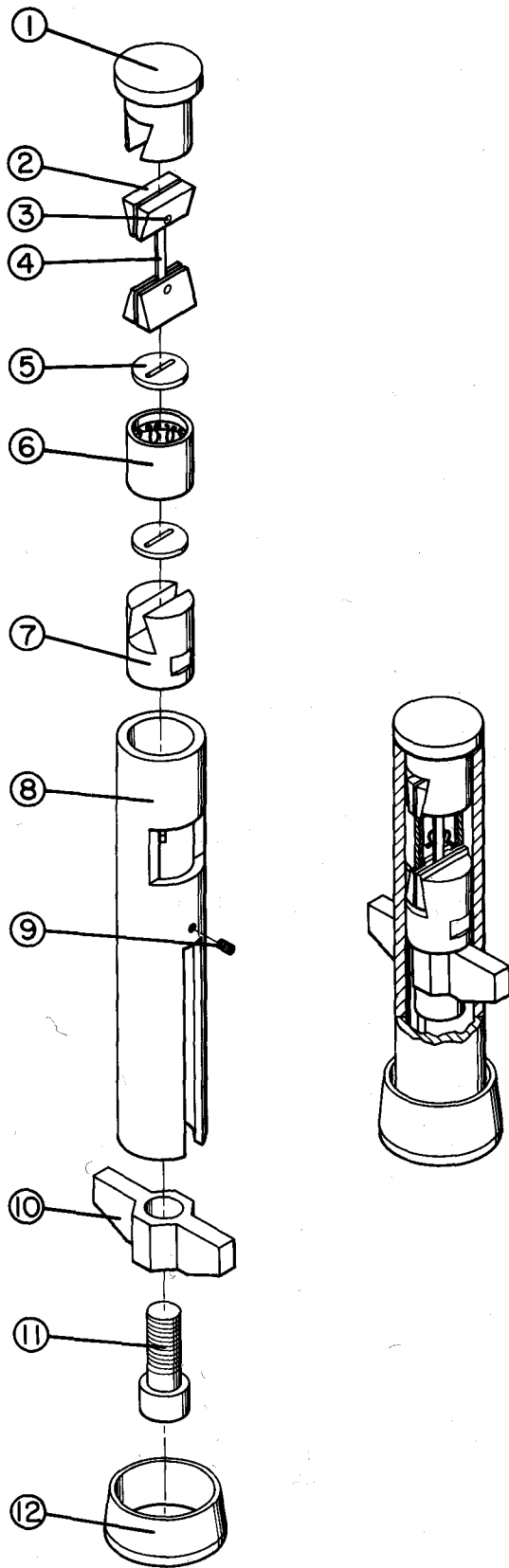
Fig. 1 — Schematic diagram of the high-rate tensile test in the two-inch gas gun.

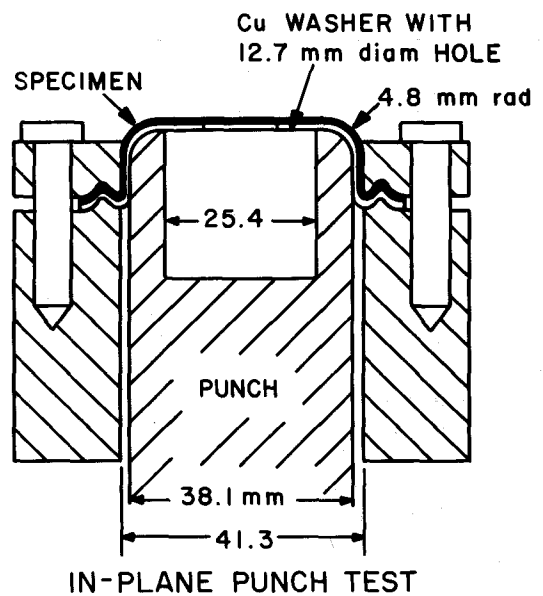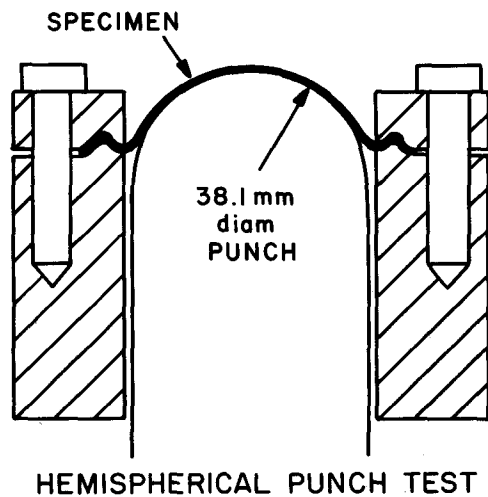HEMISPHERICAL PUNCH TEST

IN-PLANE PUNCH TEST

Fig. 2 — Schematic diagrams of the biaxial punch tests for (a) hemispherical punch test, (b) in-plane punch test.

die set at 45 m per second. Penetration is controlled by a tapered brass sleeve, shrunk-fit onto the projectile, which is jammed into a tapered catch tube. With this technique the strain rate does not remain constant during the test, but it should nevertheless average approximately 10^3 per second.

In addition to the balanced biaxial strain condition, we also tested many specimens at strain ratios intermediate between uniaxial tension and balanced biaxial tension. The punch-stretch technique was used with different specimen widths and lubricants.[21] The strain states are best represented in a strain space diagram, as shown in Figure 3. Each of the strain paths, varying from uniaxial tension at the left to balanced biaxial tension at the right, represents a specimen for which the formation of martensite was measured magnetically as a function of increasing strain.
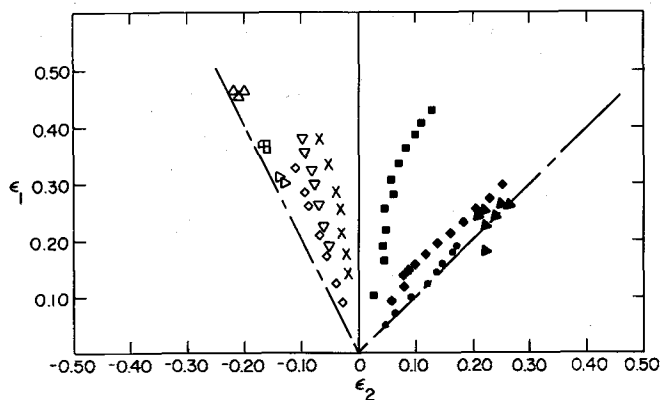
Fig. 3—Strain space diagram of strain paths in terms of maximum principal surface strain (ε_1) and minimum principal surface strain (ε_2). Each type of symbol denotes a specific strain path. Uniaxial tension is on the left, and balanced biaxial tension on the right.

B. Magnetic Measurements

The α' product of the $\gamma \to \alpha'$ martensite transformation is ferromagnetic and is readily detected by magnetic measurements. We measured magnetic permeability of specimens with a commercially available Ferritescope,* which is

---

*Model A, type EN-8-Fe, Twin City Testing Corporation, Tonawanda, New York.

---

calibrated to measure the ferrite content in weldments. A two-point probe forms a closed magnetic circuit when it is placed on the specimen and energized by a low-frequency magnetic field. The voltage induced in the probe coil by this field is a direct measure of permeability. Most of our measurements were made after deformation on portions of the test specimens where the strain levels were known accurately from circle grid measurements. Some measurements were made in situ during testing by mounting the probe on the specimen. Hence, we were able to obtain a precise measure of the permeability as a function of strain. However, the permeability of a ferromagnetic material varies with strain. This strain effect can be eliminated in a modest magnetic field at low temperatures where the atomic magnetic moments are all aligned. Hence, the moments can be "counted" by a magnetic saturation measurement and the magnetic fraction calculated very accurately. The only uncertainty is in the moment that the non-iron elements possess in an iron environment. Fortunately, this contribution is not large. We found that we could calibrate the Ferritescope readings with separate saturation magnetization measurements. Our calibration is restricted to the 304 alloy composition used.

Magnetization measurements were performed in a vibrating sample magnetometer at a temperature of $-210\ °C$, and the data from magnetic fields of 3kOe to 47kOe were used to fit a saturation curve. There was only a few pct increase in magnetization from room temperature down to $-210\ °C$, which showed that the cooling did not induce further transformation. The thin samples were measured with the applied field parallel to the sample so that demagnetizing fields were negligible. The magnetization

curves were fit to the function $m = aH + b + c/H$, which worked well for our range of magnetic fields, H. The coefficient a accommodates the linear H dependence of the unconverted austenite, b is the high-field saturation of the magnetization, and c accounts for the first order of the approach to saturation. The saturation moment for magnetic iron is $2.22\mu_B$/atom (222 emu/g), where μ_B is the Bohr magneton. For nickel and chromium in an iron host we used 133 emu/g and 0 to -75.2 emu/g, respectively.[22] Hence, the saturation magnetization for pure α' is calculated to be 175 to 154 emu/g. Although this uncertainty arises principally from the chromium moment, it is a reasonable estimate of the total uncertainty of the various moments in the alloy and is the only significant uncertainty in these magnetic measurements. The volume fraction is then calculated from the coefficient b in our fit and used to construct the calibration curve shown in Figure 4 for the Ferritescope, which we used to convert all Ferritescope readings to true volume fractions ferrite (martensite).

IV. RESULTS AND DISCUSSION

A. Uniaxial Tests

The volume fraction of α' as measured magnetically for uniaxial tensile tests at temperatures between -80 and $50\ °C$ are shown in Figure 5. The room temperature data were determined both by in situ measurements during deformation and measurements after deformation. All off-room temperature measurements were made after deformation to various strain levels. The results are also compared to those of Angel.[1] Our material is somewhat more unstable near room temperature. We have analyzed the data in a manner similar to that used by Olson and Cohen[17] for the Angel data. The parameters α and β of Eqs. [1] and [4] are plotted in Figure 6 and are compared to Olson and Cohen's results.

The constant n was chosen as 4.5, the same as that used by Olson and Cohen. These curves emphasize the strong temperature dependence of the $\gamma \to \alpha'$ transformation in the vicinity of room temperature.

The results of α' formation at high strain rate are compared to the low strain-rate room temperature data in Fig-
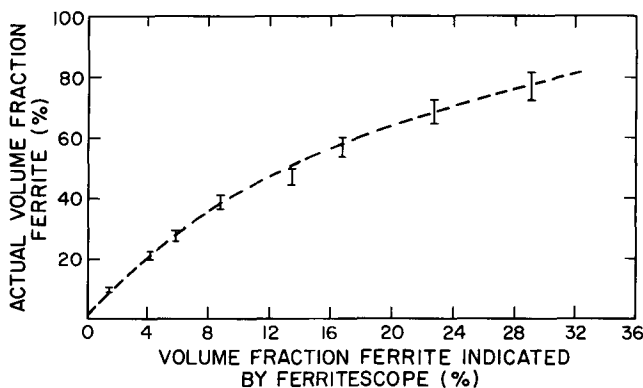

Fig. 4—Calibration curve of actual volume fraction of ferrite (martensite) as determined by saturation magnetization measurements vs ferrite, indicated by Ferritescope.
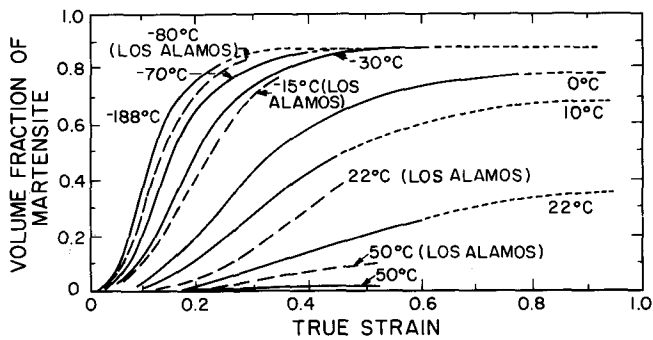
Fig. 5 — Volume fraction of martensite (α') formed during uniaxial tension as a function of true strain at different temperatures. Solid lines are data from Angel,[1] and dots are Olson-Cohen extrapolation. Dashed lines are current data.
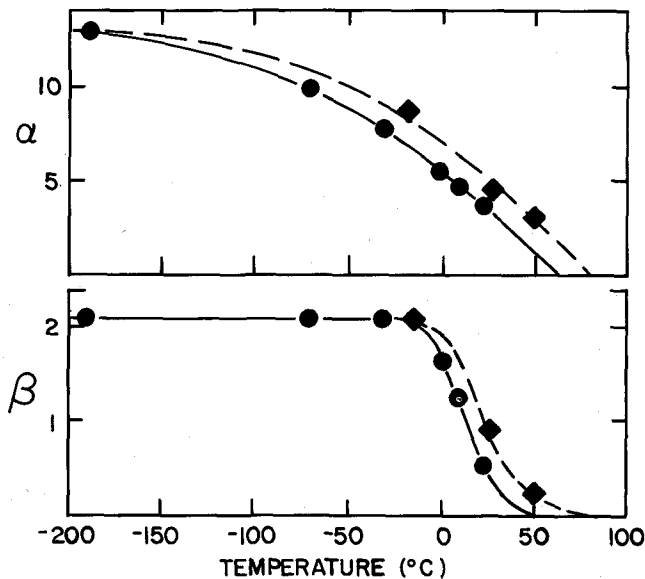

Fig. 6 — Olson-Cohen parameters α and β from Eq. [4] as a function of temperature. Solid circles represent analysis for the data of Angel. Diamonds indicate analysis for present data.

Fig. 7 — Actual volume fraction of martensite formed during straining at room temperature in uniaxial tension at high (10^3/s) and low (10^{-3}/s) strain rates.

levels, causing increased α' production. At larger strains, the temperature rise decreases the value of β sufficiently to suppress the formation of martensite in spite of the greater number of shear-band intersections. In fact, at a strain of 0.4 the amount of α' formed at high rate and room temperature is close to that formed at low rate and 50 °C. We were not able to get good total elongations at high rate because of the tendency for these specimens to break outside the gage length.

B. Biaxial Tests

The volume fraction of α' was measured as a function of increasing principal surface strain for specimens deformed in balanced biaxial tension ($\varepsilon_1 = \varepsilon_2$). The results are compared to those of uniaxial tension in Figure 8. It is quite apparent that for this strain comparison, biaxial tension is much more effective in inducing the $\gamma \rightarrow \alpha'$ transformation. However, one must ask the question of what is the proper choice of strain measure for comparison. Intuition suggests that it should be similar to the effective strain criteria used to correlate uniaxial and biaxial hardening. Although the Olson-Cohen analysis considers only uniaxial tensile

ure 7. At strain levels <0.25, high rates produce more α', whereas at larger strains, the trend is reversed. The Olson-Cohen analysis through the parameter α predicts an increase in the amount of martensite with increasing rate because of increased shear band formation. However, any significant increase in temperature resulting from adiabatic heating decreases β, as shown in Figure 6, and thereby decreases the tendency for α' formation. Several tensile specimens were tested with thermocouples spot welded to the specimen to measure the temperature rise. At low strain rates the increase in temperature was less than one degree centigrade. At high rates the average increase measured for specimens deformed to approximately 30 pct strain was 40 °C. The deformation occurred over ~230 μs and the thermocouples registered most of the 40 °C temperature rise during the last 120 μs.

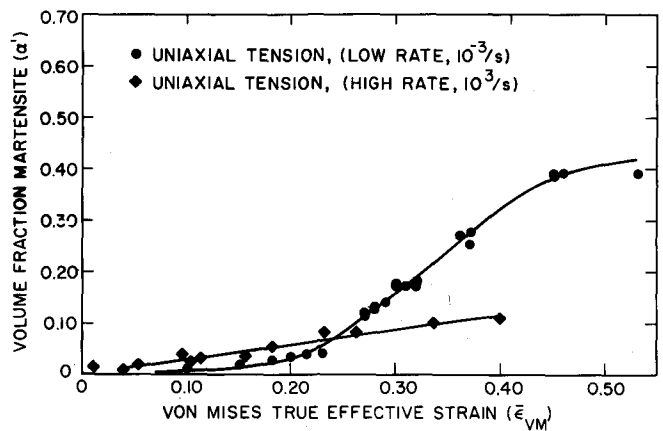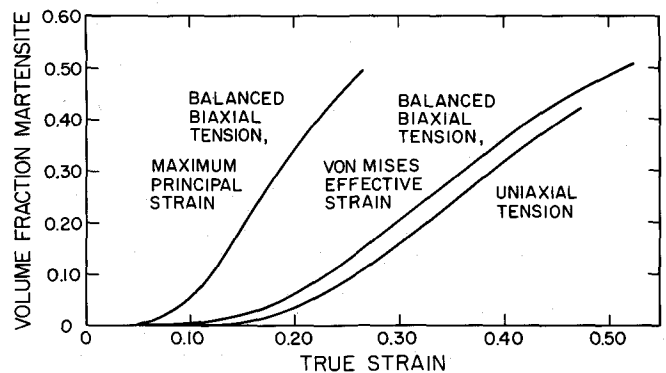Our results indicate that during high-rate deformation the increased number of shear bands predominate at small strain

Fig. 8 — Comparison of actual volume fraction of martensite formed at room temperature during uniaxial and balanced biaxial tension. Use of von Mises effective strain instead of maximum principal strain shifts the curves into much better agreement.

deformation, we can gain some insight from their analysis. Eq. [1] describes the rate of shear band formation with strain. The factors that influence this rate also influence strain hardening and, hence, it seems appropriate to use an effective strain criterion and replace ε in Eq. [1] with $\bar{\varepsilon}$. The number of intersections (Eq. [2]) depends on the number of operative slip systems and when they begin to operate during deformation. This is difficult to assess; however, we will assume it is similar to uniaxial tension, in which case the constant n would be the same. The probability p and the parameter β depend on the state of stress. In 304 stainless steel the transformation is principally strain-induced rather than stress-assisted and, hence, we expect the stress state effect to be small. Also, the thin sheet used in this investigation precludes any stress buildup in the thickness direction, thereby limiting the magnitude of the hydrostatic tensile stress component. Therefore, the principal effect of biaxial tension on the $\gamma \rightarrow \alpha'$ transformation should be accounted for by using the proper effective strain criterion in Eq. [1].

The most commonly used effective strain criteria for plastic deformation are the von Mises, Hill, and Tresca criteria. The effective strain for the von Mises criterion is given by

$$\bar{\varepsilon}_{VM} = \frac{\sqrt{2}}{3}[(\varepsilon_1 - \varepsilon_2)^2 + (\varepsilon_2 - \varepsilon_3)^2 + (\varepsilon_3 - \varepsilon_1)^2]^{1/2} \quad [5]$$

Hill's correction for anisotropy is very small because this 304 stainless steel is nearly isotropic with a measured plastic anisotropy ratio (R) of 0.9. The Tresca, or maximum shear stress, criterion is defined by

$$\bar{\varepsilon}_T = (\varepsilon_1 - \varepsilon_3) \quad [6]$$

For the case of balanced biaxial tension ($\varepsilon_1 = \varepsilon_2$), the von Mises and Tresca criteria coincide, $i.e.$, $\bar{\varepsilon} = 2\varepsilon_1$. A comparison of volume fraction α' vs strain based on an effective strain comparison is also shown in Figure 8. The uniaxial curve remains unchanged because $\bar{\varepsilon} = \varepsilon_1$, whereas the balanced biaxial curve is now shifted into reasonable agreement with the uniaxial data. We also note that for balanced biaxial tension the effective strain equals the thickness strain because of the constancy of volume condition.

In an attempt to distinguish between the von Mises and Tresca criteria, we ran tests at strain ratios between those of uniaxial and balanced biaxial tension. The ratios are shown in Figure 3. The results from magnetic measurements of volume fraction α' for these strain ratios are plotted in terms of the von Mises and Tresca effective strain criteria in Figures 9(a) and 9(b). Better agreement is observed for the von Mises criterion, which also typically provides a better correlation of plastic flow with stress state.[23]

Figure 9(a) shows that the Olson-Cohen model, with the von Mises effective strain replacing uniaxial strain, provides a reasonable prediction for the amount of deformation-induced martensite under a general, complex stress state. However, as shown in Figures 8 and 9(a), balanced biaxial tension still produces more martensite. Hence, either the number of shear band intersections are different (n varies with stress state) or the increased hydrostatic tensile component in biaxial tension increases the thermodynamic driving force sufficiently (per the analysis of Patel and Cohen[16]). This difference in martensite production will be considered in Part II.
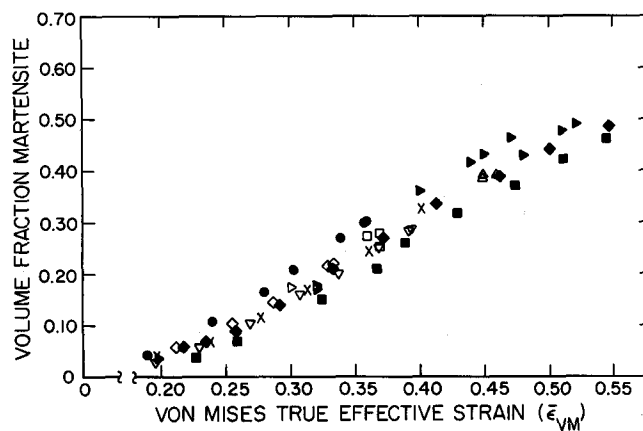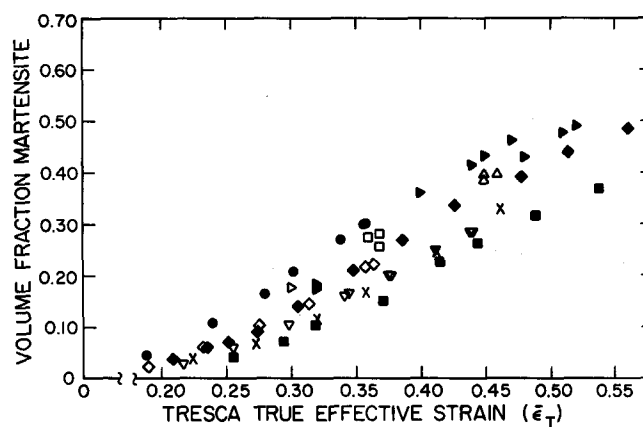
Fig. 9—Actual volume fraction of martensite formed during deformation at a variety of strain ratios. The symbols correspond to the strain paths in Figure 3. (a) Strain comparison is based on von Mises effective strain criterion and (b) on Tresca criterion.

The amount of transformation induced during high-rate biaxial tension compared to low-rate biaxial tension is shown in Figure 10. It was not possible to distinguish between high rate and low rate at strain levels <0.2, whereas at larger strains the rate of α' formation was considerably
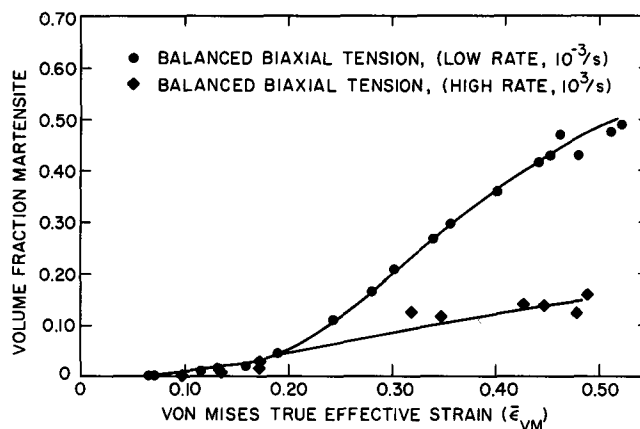

Fig. 10—Actual volume fraction of martensite formed during straining at room temperature in balanced biaxial tension at high (10^3/s) and low (10^{-3}/s) strain rates.

less at high rates. Although we made no temperature measurements on biaxial specimens, we expect a similar temperature increase to that in uniaxial tension and a similar tendency for reduced martensite formation. The von Mises effective strain criterion again gives good agreement for the comparison of martensite formation at high strain rates (Figure 7 compared with Figure 10).

V. MECHANICAL RESPONSE

The high work hardening rates and large total elongations of austenitic stainless steels are of great interest for many structural and metal forming applications. The true stress – true strain curves for our 304 stainless steel tested at four different temperatures are shown in Figure 11. Strain hardening at 22 °C is slightly greater than that observed at 50 °C. The difference becomes significant only at strains exceeding 0.25, at which point we find substantial formation of α' at 22 °C. These results suggest that the high initial strain hardening rate is a result primarily of low stacking fault energy and the resultant planar slip geometry. However, transformation occurs, which increases the hardening rate such that the stress-strain curve actually shows an inflection at strains of ~0.1. This increased hardening rate is similar to that observed for TRIP steels.[24,25]

However, at larger strains the transformation saturates (see Figure 5) and the strain hardening rate decreases dramatically, resulting in premature plastic instability (necking). Consequently, the total elongations are low at these temperatures. The principal requirements for high elongation appears to be continued transformation during deformation. This will result in maximum elongation at a temperature between M_s and M_d. Similar results have been reported by Tamura, Maki, and Hato.[15]

Instability and failure in sheet materials subjected to biaxial tension has been a subject of intense interest in recent years.[26,27] Hecker[28] has previously reported the limiting strain curve for the 304 stainless steel studied in this investigation. The results are reproduced in Figure 12. Unlike limit strain curves denoting the onset of localized necking for most other materials,[28] the curve for 304 stainless steel shows a distinct maximum on the right-hand side (biaxial
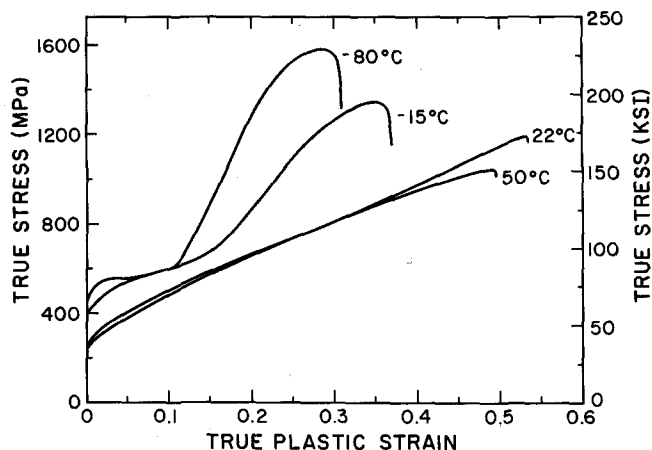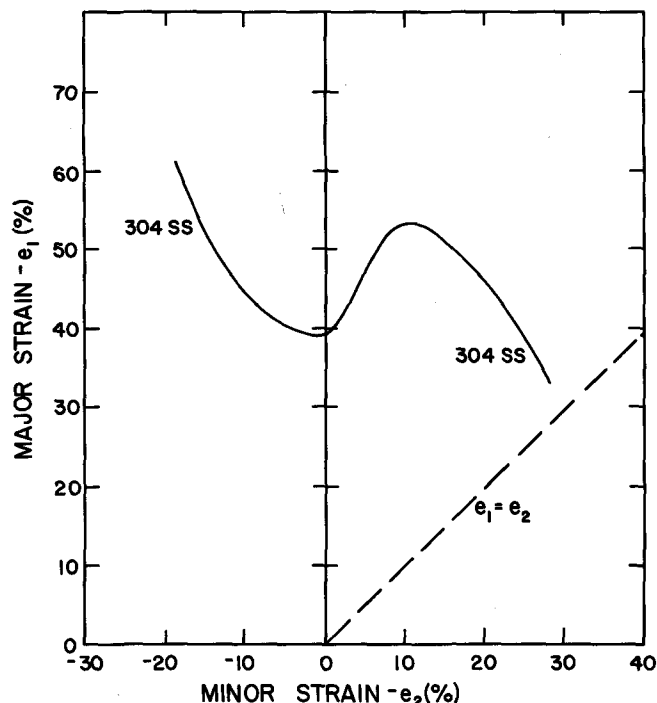
Fig. 12—Failure limit diagram for our 304 stainless steel sheet from Ref. 28. Failure denoted by this curve represents the onset of localized necking. Near balanced biaxial tension on the right-hand side, necking could not be distinguished from fracture.

stretching). We now propose that in biaxial tension (beyond the maximum in Figure 12), the work hardening rate drops because the $\gamma \rightarrow \alpha'$ transformation begins to slow down. This occurs because in biaxial tension the amount of martensite formed *per* principal surface strain is more than twice that in uniaxial tension (see Figure 8). Hence, we view the deformation near balanced biaxial tension similar to low-temperature uniaxial deformation. The initially rapid $\gamma \rightarrow \alpha'$ transformation cannot be sustained to large strains, and premature local plastic instability results.

It is worthwhile to explore another possibility for low ductility. Bressanelli and Moskowitz[9] proposed that decreased uniaxial ductility at low temperatures results from premature fracture because of the limited ductility of the martensite product. For 304 stainless steel the martensitic product is bcc rather than tetragonal and, hence, is not necessarily brittle. In fact, all tensile specimens exhibited diffuse necking before failure. Final failure at low temperatures occurred by macro-shear band localization. Examination of fracture surfaces by scanning electron microscopy also showed all fractures to be of the ductile dimple type, with no indications of brittle cleavage. In biaxial tension it is not possible to determine if plastic instability precedes fracture in such thin sheets. However, all fracture surfaces exhibited ductile dimple failure only. Therefore, we conclude that the premature fracture argument is not valid in the current work.

VI. CONCLUSIONS

1. The kinetics of strain-induced $\gamma \rightarrow \alpha'$ transformation in 304 stainless steel sheet deformed in uniaxial tension are

Fig. 11—True stress – true strain curves at four temperatures at a strain rate of 10^{-3}/s.

described well by the Olson-Cohen analysis. The volume fraction of α' is a sigmoidal function of strain and the transformation is very sensitive to temperature in the vicinity of room temperature.

2. At low strain levels, α' forms more readily during high-rate uniaxial tension ($\sim 10^3$ per second) than low-rate uniaxial tension (10^{-3} per second). This is as expected from the Olson-Cohen analysis. However, at strains greater than 0.25, the temperature rise resulting from adiabatic heating reduces the driving force for $\gamma \rightarrow \alpha'$ and, consequently, the rate of α' formation is considerably less at high rates.

3. Under a general stress (or strain) state the Olson-Cohen analysis can be extended to give reasonable predictions of the kinetics of the $\gamma \rightarrow \alpha'$ transformation by using the von Mises effective strain in place of the uniaxial strain. We found that in balanced biaxial tension, more than twice as much martensite forms per maximum principal strain as in uniaxial tension.

4. The strain-induced $\gamma \rightarrow \alpha'$ transformation increases the strain hardening rate as expected at $-15\ °C$ and $-80\ °C$. However, the total elongations to failure decrease. We found that failure occurs prematurely as a result of saturation of martensite formation at large strains, which decreases the strain hardening rate.

5. In biaxial tension, a similar tendency for saturation exists at room temperature, resulting in a decreased strain hardening rate and premature instability, which might explain the low biaxial ductility of our 304 stainless steel.

ACKNOWLEDGMENTS

REFERENCES

1. T. Angel: *J. Iron Steel Inst.*, 1954, vol. 177, p. 165.
2. B. Cina: *J. Iron Steel Inst.*, 1954, vol. 177, p. 406.
3. J. A. Venables: *Phil. Mag.*, 1962, vol. 7, p. 35.
4. R. Lagneborg: *Acta Met.*, 1964, vol. 12, p. 823.
5. G. W. Powell, E. R. Marshall, and W. A. Backofen: *Trans. ASM*, 1958, vol. 50, p. 479.
6. C. J. Guntner and R. P. Reed: *Trans. ASM*, 1962, vol. 55, p. 399.
7. P. L. Manganon and G. Thomas: *Metall. Trans.*, 1970, vol. 1, p. 1577.
8. J. Dash and H. M. Otte: *Acta Met.*, 1963, vol. 11, p. 1169.
9. J. P. Bressanelli and A. Moskowitz: *Trans. ASM*, 1966, vol. 59, p. 223.
10. G. B. Olson and M. Cohen: *J. Less-Common Metals*, 1972, vol. 28, p. 107.
11. P. C. Maxwell, A. Goldberg, and J. C. Shyne: *Metall. Trans.*, 1974, vol. 5, p. 1305.
12. K. Mathieu: *Mitteilungen aus dem Kaiser Wilhelm Inst. für Eisenforschung*, 1942, vol. 24, p. 243.
13. G. W. Form and W. M. Baldwin, Jr.: *Trans. ASM*, 1956, vol. 48, p. 474.
14. D. V. Neff, T. E. Mitchell, and A. R. Troiano: *Trans. ASM*, 1969, vol. 62, p. 858.
15. I. Tamura, T. Maki, and H. Hato: *J. Jap. Inst. Metals*, 1969, vol. 33, p. 1376.
16. J. R. Patel and M. Cohen: *Acta. Met.*, 1953, vol. 1, p. 531.
17. G. B. Olson and M. Cohen: *Metall. Trans. A*, 1975, vol. 6A, p. 791.
18. P. M. Kelly and J. Nutting: *J. Iron Steel Inst.*, 1961, vol. 184, p. 199.
19. E. Lecroisey and A. Pineau: *Metall. Trans.*, 1972, vol. 3, p. 387.
20. C. E. Frantz and S. S. Hecker: LASL Report 6258, November 1976, Los Alamos Scientific Laboratory, Los Alamos, NM 87545.
21. S. S. Hecker: *Sheet Met. Ind.*, November 1975, p. 671.
22. Mary Beth Sterns: *Phys. Rev. B.*, 1976, vol. 13, p. 1183.
23. S. S. Hecker: *Constitutive Equations in Viscoplasticity: Computation and Engineering Aspects*, Am. Soc. Mech. Engrs., 1976, p. 1.
24. V. F. Zackay, E. R. Parker, D. Fahr, and R. Busch: *Trans. ASM*, 1967, vol. 60, p. 252.
25. G. B. Olson and M. Azrin: *Metall. Trans. A*, 1978, vol. 9A, p. 713.
26. D. P. Koistinen and N. M. Wang, eds., *Mechanics of Sheet Metal Forming: Material Behavior and Deformation Analysis*, Plenum Press, 1978.
27. S. S. Hecker, A. K. Ghosh, and H. L. Gegel, eds., *Formability: Analysis, Modeling and Experimentation*, TMS-AIME, 1978.
28. S. S. Hecker: *Formability: Analysis, Modeling and Experimentation*, TMS-AIME, 1978, p. 150.